Supplementary Information:
Extreme Ultraviolet Second Harmonic Generation Spectroscopy in a Polar Metal

Emma Berger[1,2,*], Sasawat Jamnuch[3], Can B. Uzundal[1,2], Clarisse Woodahl[4], Hari Padmanabhan[5], Angelique Amado[1,2], Paul Manset[6], Yasuyuki Hirata[7], Yuya Kubota[8,9], Shigeki Owada[8,9], Kensuke Tono[8,9], Makina Yabashi[8,9], Cuixiang Wang[10], Youguo Shi[10], Venkatraman Gopalan[5], Craig P. Schwartz[11], Walter S. Drisdell[11,12], Iwao Matsuda[13,14], John W. Freeland[15], Tod A. Pascal[3,16,17], Michael Zuerch[1,2,18,19,*]

1. Department of Chemistry, University of California, Berkeley, California 94720, USA
2. Materials Sciences Division, Lawrence Berkeley National Laboratory, Berkeley, California 94720, USA
3. ATLAS Materials Science Laboratory, Department of Nano Engineering and Chemical Engineering, University of California, San Diego, La Jolla, California, 92023, USA
4. University of Florida, Gainesville, FL 32611, USA
5. Department of Materials Science and Engineering, The Pennsylvania State University, University Park, Pennsylvania 16801, USA
6. Ecole Normale Superieure de Paris, Paris, France
7. National Defense Academy of Japan, Yokosuka, Kanagawa 239-8686, Japan
8. RIKEN SPring-8 Center, Sayo, Hyogo 679-5148, Japan
9. Japan Synchrotron Radiation Research Institute (JASRI), Sayo, Hyogo 679-5198, Japan
10. Institute of Physics, Chinese Academy of Sciences, Beijing 100190, China
11. Chemical Sciences Division, Lawrence Berkeley National Laboratory, Berkeley, California 94720, USA
12. Joint Center for Artificial Photosynthesis, Lawrence Berkeley National Laboratory, Berkeley, California 94720, USA
13. Institute for Solid State Physics, The University of Tokyo, Kashiwa, Chiba 277-8581, Japan
14. Trans-scale Quantum Science Institute, The University of Tokyo, Bunkyo-ku, Tokyo 113-0033, Japan
15. X-ray Science Division, Argonne National Laboratory, Argonne, IL 60439, USA
16. Materials Science and Engineering, University of California San Diego, La Jolla, California, 92023, USA
17. Sustainable Power and Energy Center, University of California San Diego, La Jolla, California, 92023, USA
18. Fritz Haber Institute of the Max Planck Society, 14195 Berlin, Germany
19. Friedrich Schiller University, 07743 Jena, Germany

Section S0: Methods

Experimental setup

The experiment was conducted at the BL1 beamline at SACLA[1]. The 30-fs, p-polarized XFEL was passed through a 0.8 μm Al filter used to attenuate the beam to prevent sample damage and focused onto the [120] plane of $LiOsO_3$ at an angle of 45° with respect to the surface normal to a spot size with full-width-half-maximum (FWHM) of 50 μm. The reflected fundamental XFEL beam was orders of magnitude attenuated due to its incidence at Brewster's angle. The presence of any reflectivity at Brewster's angle can be attributed to either slight polarization contamination or imperfect beam alignment. The reflected XUV-SHG signal and weak fundamental FEL beams were passed through a 200 μm slit and spectrally dispersed using a 1200 groove/mm grating (30-002, Shimadzu) onto a micro-channel plate (MCP) detector (Rectangular, Hamamatsu Photonics) coated with CsI. The resulting images were captured with a camera (IPX-VGA120-LMCN, Imperx Inc.). An approximate 0.2% photon energy jitter was harnessed to increase spectral resolution. Shot-to-shot intensity fluctuations in the fundamental intensity were used to extract the second-order susceptibility. Experiments were carried out below T_c at 62 K with ten different incident energies ranging from 28-33 eV[1] and above T_c at 160 K, though no signal above signal-to-noise limit was detected in this latter experiment.

Data Processing

Each shot was registered on the MCP detector as a 2D image containing the fundamental peak and the second harmonic peak at frequencies of ω and 2ω, respectively. Shots of poor quality were identified as those with a full-width half-maximum (FWHM) at the fundamental frequency greater than 1.5 standard deviations away from the average FWHM and discarded. The remaining spectra were background corrected, binned, and averaged according to the energy and intensity of the incident laser pulse. Within each bin, the average intensity of the fundamental and second harmonic peaks were extracted. A linear function was fit to the linearized $I(\omega)$ vs. $|I(2\omega)|^2$ plot at each incident energy to extract the nonlinear

susceptibility according to equation (1) as shown in Figure S1.2. Further details on the spectral analysis can be found in Section S1 of the supplementary materials. This process was then repeated at all incident energies to produce a modulo $\chi^{(2)}$ spectrum. To compare experiment with theory, a 35.4 eV rigid shift in the TDDFT energy axis was determined to be necessary. The magnitude of the shift was chosen by finding the best fit to the experimental results. Such a treatment has been shown to be a valid approximation under the assumption that $\chi^{(2)}$ spectrum lineshapes are the same at the second-order response of the fundamental and first-order response of the SHG and differ only by an additive offset.[2]

Sample

Single crystals of $LiOsO_3$ were prepared using a solid-state reaction at high pressure, as outlined by Shi *et al.*[3]. The crystals were hand-polished using calcined alumina polishing paper of roughness 0.3 μm. The surface roughness may have reduced the overall signal due to off-axis scattering given the roughness-to-wavelength ratio. However, the additional surface area did not contribute noticeable surface SHG as it would have been observed in the high temperature measurement. Electron back-scattering diffraction was then used to orient the crystals and confirm crystallinity by the procedure described in the supplementary information of reference [4]. The surface of the crystal was confirmed to be largely single-domain, with a small fraction of few micron-sized domains of contamination. The 50 μm FWHM spot size of the FEL beam was therefore at least one order of magnitude larger than the domain contamination.

Section S1: Extracting the nonlinear susceptibility from experimental data

For each XFEL shot at a particular incident energy, the detector recorded three dominant features: the specular beam reflected off the grating, and the first diffraction order of both the fundamental and second harmonic, the latter two features can be clearly seen in **Fig S1.1**. It can be noted that the second harmonic peak is broader than the fundamental. Though it is expected for the opposite to be true due to nonlinear effects, this is likely a result the flatfield grating being slightly out of focus at the second harmonic. Given that none of the conclusions are based off of pulse width, this observation should not impact any of the claims made in the main text.

For each single-shot-image, a Gaussian peak was fit to each of the three spectral features. If the FWHM of the first order diffraction peak of the fundamental was larger than 1.5 standard deviations from the mean, the shot was discarded. The Gaussian peak position of the fundamental was used to sort shots in bins by energy. The integral of the fundamental was used to sort shots into bins by incident intensity. Absolute values of energy were found via calibration using the grating equation. To extract the $\chi^{(2)}(2\omega)$ scaling with fundamental intensity value for each energy, the shots in each energy sub-bin were further binned into 64 bins with respect to the incident fundamental intensity and subsequently averaged. The average second harmonic intensity was then extracted for each bin. The respective intensities for each bin were calculated by integrating the Gaussians using the trapezoidal rule. $\chi^{(2)}(2\omega)$ was extracted by linearizing the dependence shown in Eq.(1) of the main text by plotting the square of the fundamental intensity vs. the second harmonic intensity. A linear function was fit to the linear region of this plot, with the corresponding slope reporting on the $\chi^{(2)}(2\omega)$ scaling with fundamental intensity **(Fig. S1.2).**

As can be seen from **Fig. S1.2**, the shots with low intensity of the fundamental do not seem to scale appropriately quadratically with the intensity of the second harmonic. To investigate this further, slopes were extracted across several regions of $I(\omega)$ showing linear behaviour in the linearized plot Fig. S1.2. While absolute values of $\chi^{(2)}(2\omega)$ differed, the relative relationships of all points with respect to all others was the same. This suggests that the MCP detector, which can have nonlinear behaviour as a function of intensity, has a nonlinear response function that differs at low and high intensities. Given that only relative values of $\chi^{(2)}(2\omega)$ are reported in arbitrary units, this did not impact data interpretation since consistent intensity regions were utilized to extract the $\chi^{(2)}(2\omega)$ spectrum. Finally, the more linear, high intensity region where we expect best signal-to-noise was used to extract the second-order response shown in **Fig. 2e** of the main text.

Section S2: The linear response

The absolute reflectance of $LiOsO_3$ was characterized at beamline 6.3.2 at the Advanced Light Source (ALS) at Lawrence Berkeley National Laboratory[5]. The reflectance from 20-70 eV was measured at four different incident angles with respect to the sample normal (10°, 20°, 30°, 45°). The imaginary part of the $LiOsO_3$ dielectric function, $\kappa(\omega)$, shown as a gray dashed line in **Fig. S2.1**, was extracted using the numerical algorithm as that used in the work by Kaplan *et al.*[6] The red and blue curves in the figure

correspond to the calculated linear response of the centrosymmetric and non-centrosymmetric $LiOsO_3$ phases, respectively, that are shifted by +3.15 eV to match experiment. From the theory-calculated $\kappa(\omega)$, we see the two phases have an almost identical response, which is in-line with previous calculations that show density of states (DOS) near the Fermi-level changes minimally between the two phases[7].

Section S3: Theoretical calculations of $\chi^{(2)}$

The second-order nonlinear susceptibility was calculated according to the following equation

$$\chi^{(2)}_{ijk}(2\omega;\omega+\omega) = \frac{N}{\epsilon_0\hbar^2}\sum_{nn'}\frac{\langle i\rangle_{gn}\langle j\rangle_{nn'}\langle k\rangle_{n'g}}{(\omega_{ng}-2\omega)(\omega_{n'g}-\omega)} + \frac{\langle j\rangle_{gn}\langle i\rangle_{nn'}\langle k\rangle_{n'g}}{(\omega_{ng}+\omega)(\omega_{n'g}-\omega)} + \frac{\langle j\rangle_{gn}\langle k\rangle_{nn'}\langle i\rangle_{n'g}}{(\omega_{ng}+\omega)(\omega_{n'g}+2\omega)}$$

where $\langle i\rangle, \langle j\rangle, \langle k\rangle$ represent the average electric dipole moments along the i,j, and kth Cartesian axes connecting the g, n', and n states which are indicated in the subscripts and denote the ground state, first excited state, and second excited state, respectively[8]. As can be seen from the first two terms on the right hand side of the equation, there is a strong resonant enhancement of the SHG signal when the frequency of incident light, ω, corresponds to the transition frequency between the ground and first excited states, $\omega_{n'g}$ or when it is half-resonant with the ω_{ng} transition. This particular experiment satisfies the latter condition. Within the *exciting* package, the simulation calculates the nonlinear response when a photon at the fundamental frequency is incident on the sample. In this experiment, the relevant part of the $\chi^{(2)}(2\omega)$ spectrum thus includes energies at half of the measured SHG signal. Empty states are included in the ground state calculation to account for possible transitions to higher energy states, which results in Kohm-Sham eigenvalues related to the energy levels of the sample system.

Section S4: Determining the $\chi^{(2)}_{eff}$ response[8]

In contracted notation, $d_{ijk} = \frac{1}{2}\chi^{(2)}_{ijk}$. where the contracted matrix notation $d_{ijk} = d_{il}$ is given by the Voigt notation. The nonlinear susceptibility tensor for the R3c symmetry group has only 4 independent terms:

$$d_{il} = \begin{bmatrix} 0 & 0 & 0 & 0 & d_{15} & d_{16} \\ d_{16} & -d_{16} & 0 & d_{15} & 0 & 0 \\ d_{31} & d_{31} & d_{33} & 0 & 0 & 0 \end{bmatrix} \quad (1)$$

This matrix defines the polar axis along the z axis, while the experiment was performed with the polar axis perpendicular to the z-axis as defined in the experimental frame of reference **(Figure S4.1).** Note that in all other portions of the manuscript, the z-axis is chosen to be the hexagonal 3-fold axis of rotation, but the convention is changed just for section S4 since, here, the z-axis is defined to be normal to the sample surface. To account for this, the d_{il} tensor was rotated by 90° about the y-axis to give the rotated d'_{il} tensor:

$$d_{il} = \begin{bmatrix} -d_{33} & -d_{31} & -d_{31} & 0 & 0 & 0 \\ 0 & -d_{16} & -d_{16} & 0 & 0 & d_{15} \\ 0 & 0 & 0 & -d_{16} & -d_{15} & 0 \end{bmatrix} \quad (2)$$

With this tensor, the second-order polarization response of the medium was calculated:

$$P_i(2\omega) = 2\varepsilon_0 d'_{il} E_j(\omega) E_k(\omega) \quad (3)$$

where i,j,k correspond to the x,y,z coordinate axes. The geometry of the experiment as shown in **Figure S4.1** is such that the incident beam makes an angle θ=45° with the z-axis and an angle φ=240° with the x-axis when projected into the xy-plane. The electric field of the incident photon at the fundamental frequency can then be decomposed into

$$\begin{bmatrix} E_x(\omega) \\ E_y(\omega) \\ E_z(\omega) \end{bmatrix} = \begin{bmatrix} -E_0 \sin\theta\cos\phi \\ -E_0 \sin\theta\sin\phi \\ -E_0\cos\theta \end{bmatrix} = \frac{E_0}{\sqrt{2}} \begin{bmatrix} 1/2 \\ \sqrt{3}/2 \\ -1 \end{bmatrix} \quad (4)$$

where E_0 is the amplitude of the incoming electric field. Substituting equations (2) and (4) into (3) gives the induced polarization

$$\vec{P} = \begin{bmatrix} P_x(2\omega) \\ P_y(2\omega) \\ P_z(2\omega) \end{bmatrix} = -\epsilon_0 \frac{E_0^2}{4} \begin{bmatrix} d_{33} + 7d_{31} \\ -2\sqrt{3}d_{15} - d_{16} \\ -4\sqrt{3}d_{16} - 4d_{15} \end{bmatrix} \quad (5)$$

To determine the polarization the detector sees, the polarization vector needs to be decomposed into two parts that carry polarization parallel and perpendicular to the wave vector of the reflected beam. Since a traveling photon can only have transverse polarization, the detector only measures the $\| P_\perp \|$ component. In spherical coordinates, the outgoing reflected beam lies along the vector $(r, \theta, \phi) = (1, 45°, 60°)$. In Cartesian coordinates, this is the vector $\vec{R} = \left(\frac{1}{2\sqrt{2}}, \frac{\sqrt{3}}{2\sqrt{2}}, \frac{1}{\sqrt{2}}\right)$ with a norm of 1. The projection of $\vec{P}$ onto $\vec{R}$ is

$$P_\parallel = \text{proj}_{\vec{R}}\vec{P} = (\vec{R} \cdot \vec{P})\vec{R} = \left(\frac{P_x}{8}, \frac{3P_y}{8}, \frac{4P_z}{8}\right) \quad (6)$$

The perpendicular component is then

$$\begin{aligned} P_\perp &= \vec{P} - \vec{P}_\parallel = \left(\frac{7P_x}{8}, \frac{5P_y}{8}, \frac{4P_z}{8}\right) \\ &= -\frac{\epsilon_0 E_0^2}{32}(7d_{33} + 49d_{31}, -10\sqrt{3}d_{15} - 5d_{16}, -16\sqrt{3}d_{16} - 16d_{15}) \quad (7) \\ \| P_\perp \| &= \frac{\epsilon_0 E_0^2}{32}(49d_{33}^2 + 2401\, d_{31}^2 + 556d_{15}^2 + 793\, d_{16}^2 + 686 d_{31}d_{33} + 612\sqrt{3}d_{15}d_{16})^{1/2} \end{aligned}$$

therefore

$$d_{\text{eff}} = \frac{1}{32}(49d_{33}^2 + 2401\, d_{31}^2 + 556d_{15}^2 + 793\, d_{16}^2 + 686\, d_{31}d_{33} + 612\sqrt{3}d_{15}d_{16})^{1/2}. \quad (8)$$

Section S5: Neglecting the transient response of the FEL during the duration of the pulse

It is important to consider whether the Li ion could potentially be displaced within the envelope of the incident XFEL pulse itself. If this were the case, SHG would probe a transient excited state, rather than the ground state. Such a process would occur on a few-femtosecond timescale. To clarify this, we performed a molecular dynamics simulation on the $LiOsO_3$ supercell structure consisting of 30 atoms. The Vienna Ab initio Simulation Package (VASP) was used to propagate the system with a k-point sampling grid of 2x2x2. The system was propagated for 3 ps and the trajectory of Li atom was tracked to account for its potential motion. From the simulation, we observed that the Li atom in the polar phase is displaced from its position in the non-polar phase by 0.4881±0.0036 Å **(Fig S5.1)**. This result is in the agreeable range from the experiment and from the literature reported value of Li displacement from neutron diffraction data (0.5 Å)[3]. Its position within the duration of the experiment (3 ps) was tracked as a function of time and sorted into a histogram **(Fig. S5.2)**. Within the duration of the 30 fs XFEL pulse, the Li motion varies by about 1%. As

such, since the Li motion over the pulse length is relatively small, and it can be concluded that the SHG signal is from a static Li geometry.

Section S6: Partial Density of States (PDOS) Calculations

The density of states calculation of $LiOsO_3$ was performed in exciting. The effective k-point mesh size for Brillouin zone integration *ngrdos* was set to 1000. The energy range was chosen from -1.9 to 2.0 Hartree. The spherical harmonic basis set was transformed into site symmetries which gave the physical contribution of the DOS in term of angular quantum number or the spdf orbital characteristic. The PDOS near the Li K-edge includes contributions from Li 1s orbitals, Os 5p orbitals, and Os 4f orbitals at approximately –56.6, -60.2, and -61.6 eV, respectively. The PDOS at the Fermi level is dominated by contributions from Os 5d and O 2p orbitals and significantly smaller contributions from O 2s, Li 2s, Li 2p, Os 5s, and Os 5p orbitals (**Fig. S6.1**). The selection rules for SHG, however, only allow transitions between states for which $\Delta l = 0, \pm 2$. Given the resonant enhancement expected for incident photons at the Li K-edge, transitions originating from Os 4p and 4f orbitals are not expected to complicate the signal since transitions from s-type orbitals to p- and f-type orbitals are forbidden and as shown in Fig. 3 of the main text, Os atoms are in a predominantly centrosymmetric environment, for which SHG is not allowed. Of the transitions from Li 1s states that are allowed, O 2s orbitals are below the Fermi level and are not only occupied but also inaccessible with incident photons within the 28-33 eV range used. Furthermore, contributions of Li 2s orbitals to the TDOS are 2 orders of magnitude smaller than those of Os 5d orbitals. It can therefore be reasonably assumed that the SHG signal is selective to the Li coordination environment and represents transitions mainly from Li 1s to Os 5d orbitals.

Section S7: Theoretical Calculation of $\chi^{(2)}_{eff}$ without Li 1s response

To verify that origin of second harmonic response of $LiOsO_3$ is due to the displacement of Li atoms, we explicitly excluded the Li 1s electron from the SCF calculation. In this way the nonlinear response calculation would not include the signal from Li 1s signal. The effective second order nonlinear susceptibility is shown in **Fig. S7.1**. We observed that the majority of the nonlinear response is contributed by the Li 1s electrons. The signal from other electrons while present is heavily overshadowed by that of Li 1s electrons. Therefore, the signal we're observing primarily originate from the Li 1s which in turn is enhanced by the displacement of Li atoms from centrosymmetric positions.

Section S8: Extraction of the core-level response from calculated $\chi^{(2)}_{eff}$

The interested core response has to be extracted out from the total signal since the employed calculation method includes all the electrons within the system. Fortunately, the response from valence electron behaves as a decay function of 1/Energy. In order to extract the core response from the simulated all-electron second order susceptibility, we fitted the response to a hyperbolic function of energy in the form of $A/(Energy - B)$. The resulting core response is extracted from subtraction of the raw calculated second order susceptibility with this fitted background signal (Fig. S8.1).

Section S9: Effect of OsO_6 octahedral rotation to $\chi^{(2)}_{eff}$

From the neutron diffraction experiment of $LiOsO_6$, it was reported that polar and nonpolar phase OsO_6 octahedral rotated to allow better hybridization due to the difference between Li position in the two phases [3]. We calculate the effect on the $\chi^{(2)}_{eff}$ due to different OsO_6 orientation. From the result shown in Fig. S9.1, the rotation of OsO_6 has minimal effect on the second harmonic response of the $LiOsO_3$, all the features between the two phases are very similar. Due to the sensitivity of SHG, the change in the environment of the osmium having minimal effect to $\chi^{(2)}_{eff}$ suggests that the main signal contribution arises from the Li atoms.

References

(1) Owada, S.; Togawa, K.; Inagaki, T.; Hara, T.; Tanaka, T.; Joti, Y.; Koyama, T.; Nakajima, K.; Ohashi, H.; Senba, Y.; Togashi, T.; Tono, K.; Yamaga, M.; Yumoto, H.; Yabashi, M.; Tanaka, H.; Ishikawa, T. A Soft X-Ray Free-Electron Laser Beamline at SACLA: The Light Source, Photon Beamline and Experimental Station. *J. Synchrotron Radiat.* **2018**, *25* (1), 282–288. https://doi.org/10.1107/S1600577517015685.

(2) Pascal, T. A.; Boesenberg, U.; Kostecki, R.; Richardson, T. J.; Weng, T. C.; Sokaras, D.;

Nordlund, D.; McDermott, E.; Moewes, A.; Cabana, J.; Prendergast, D. Finite Temperature Effects on the X-Ray Absorption Spectra of Lithium Compounds: First-Principles Interpretation of X-Ray Raman Measurements. *J. Chem. Phys.* **2014**, *140* (3). https://doi.org/10.1063/1.4856835.

(3) Shi, Y.; Guo, Y.; Wang, X.; Princep, A. J.; Khalyavin, D.; Manuel, P.; Michiue, Y.; Sato, A.; Tsuda, K.; Yu, S.; Arai, M.; Shirako, Y.; Akaogi, M.; Wang, N.; Yamaura, K.; Boothroyd, A. T. A Ferroelectric-like Structural Transition in a Metal. *Nat. Mater.* **2013**, *12* (11), 1024–1027. https://doi.org/10.1038/nmat3754.

(4) Padmanabhan, H.; Park, Y.; Puggioni, D.; Yuan, Y.; Cao, Y.; Gasparov, L.; Shi, Y.; Chakhalian, J.; Rondinelli, J. M.; Gopalan, V. Linear and Nonlinear Optical Probe of the Ferroelectric-like Phase Transition in a Polar Metal, LiOsO3. *Appl. Phys. Lett.* **2018**, *113* (12). https://doi.org/10.1063/1.5042769.

(5) Underwood, J. H.; Gullikson, E. M.; Koike, M.; Batson, P. J.; Denham, P. E.; Franck, K. D.; Tackaberry, R. E.; Steele, W. F. Calibration and Standards Beamline 6.3.2 at the Advanced Light Source. *Rev. Sci. Instrum.* **1996**, *67* (9), 3372–3372. https://doi.org/10.1063/1.1147338.

(6) Kaplan, C. J.; Kraus, P. M.; Gullikson, E. M.; Borja, L. J.; Cushing, S. K.; Zürch, M.; Chang, H.-T.; Neumark, D. M.; Leone, S. R. Retrieval of the Complex-Valued Refractive Index of Germanium near the M 4,5 Absorption Edge . *J. Opt. Soc. Am. B* **2019**, *36* (6), 1716. https://doi.org/10.1364/josab.36.001716.

(7) Sim, H.; Kim, B. G. First-Principles Study of Octahedral Tilting and Ferroelectric-like Transition in Metallic LiOsO3. *Phys. Rev. B - Condens. Matter Mater. Phys.* **2014**, *89* (20), 1–5. https://doi.org/10.1103/PhysRevB.89.201107.

(8) Boyd, R. W. Nonlinear Optics (3rd Edition); Academic Press, 2008; pp 69–105.

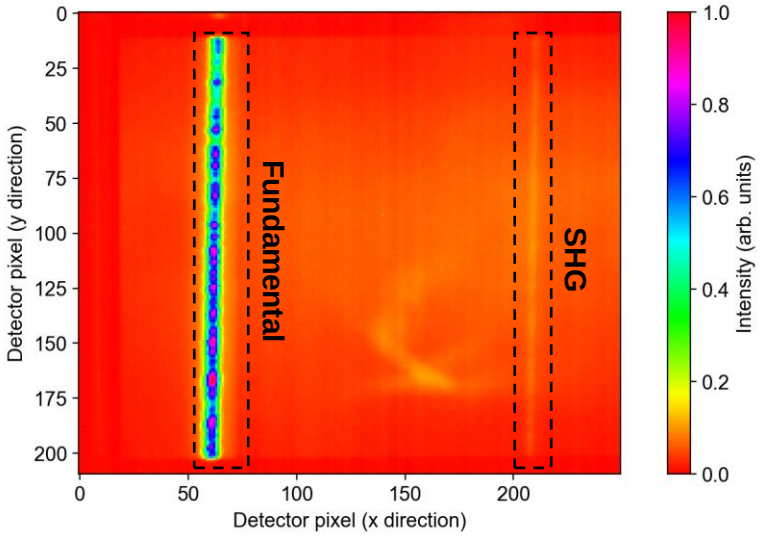

Fig. S1.1. Representative image of spectrum captured with MCP detector. All 30,000 shots at 31.5 eV were averaged together. In this image, no other modifications, including background corrections have been performed. Immediately apparent are the spectral features at the fundamental and second harmonic.

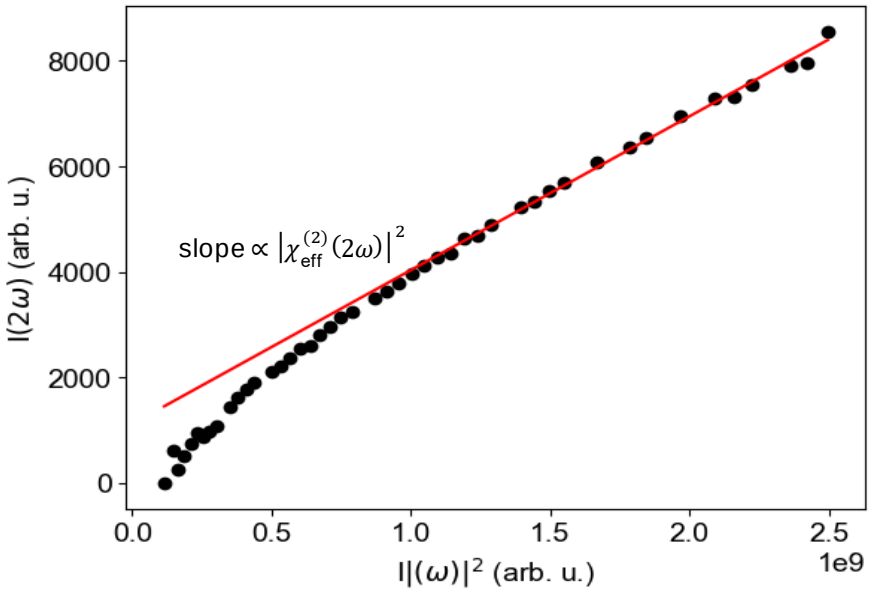

Fig. S1.2. Linear fit *to* $|I(\omega)|^2$ *vs.* $|(2\omega)$ to extract the nonlinear susceptibility $\chi^{(2)}_{\text{eff}}(2\omega)$. After sorting all the spectra according to the pixel position of the fundamental on the detector x-axis, summing all recorded intensities in the detector y-direction, and performing a background correction, integrals under the fundamental and second harmonic spectral features were calculated. With these integrals corresponding to intensity (arb. units.) the effective nonlinear susceptibility could be extracted using Eq. (1) in the main text. As an example, the linearized version of Eq. (1) is plotted here for an incident energy of 31.5 eV, indicating the slope of the linear line fit to the most linear region of the data is proportional to $|\chi^{(2)}_{\text{eff}}(2\omega)|^2$.

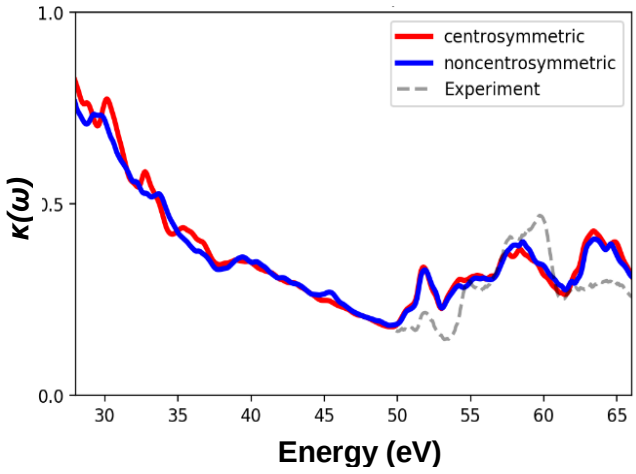

Fig. S2.1. The imaginary part of the LiOsO3 dielectric function, *κ(ω)*. Shown in red and blue are the calculated values of *κ(ω)* for the centrosymmetric and non-centrosymmetric phases. Shown with a gray dashed line is the experimentally extracted *κ(ω)* function, extracted from reflectivity data taken at the ALS. To align theory and experiment, a +3.15 eV shift in the theory x-axis was deemed necessary to best fit the data, as shown here.

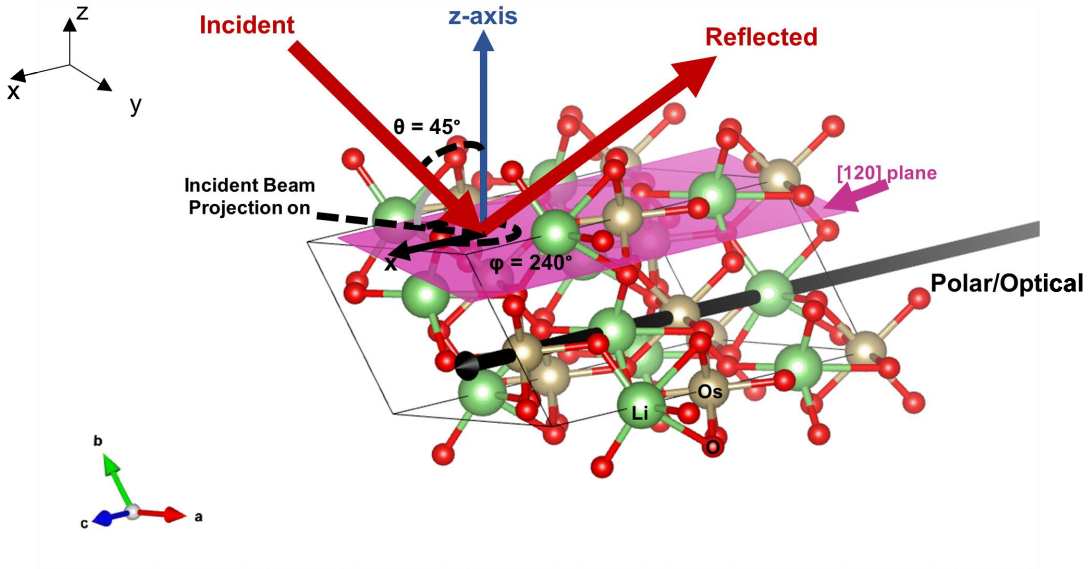

Fig. S4.1. **Experimental geometry of XUV-SHG experiment.** In the experiment, the XFEL beam was incident at 45° with respect to the [120] plane of $LiOsO_3$ (shown in pink).The projection of the incoming beam onto the xy-plane, as defined in the figure, made a 240° angle with the $LiOsO_3$ polar axis. The detector was placed at 45° with respect to the sample normal.

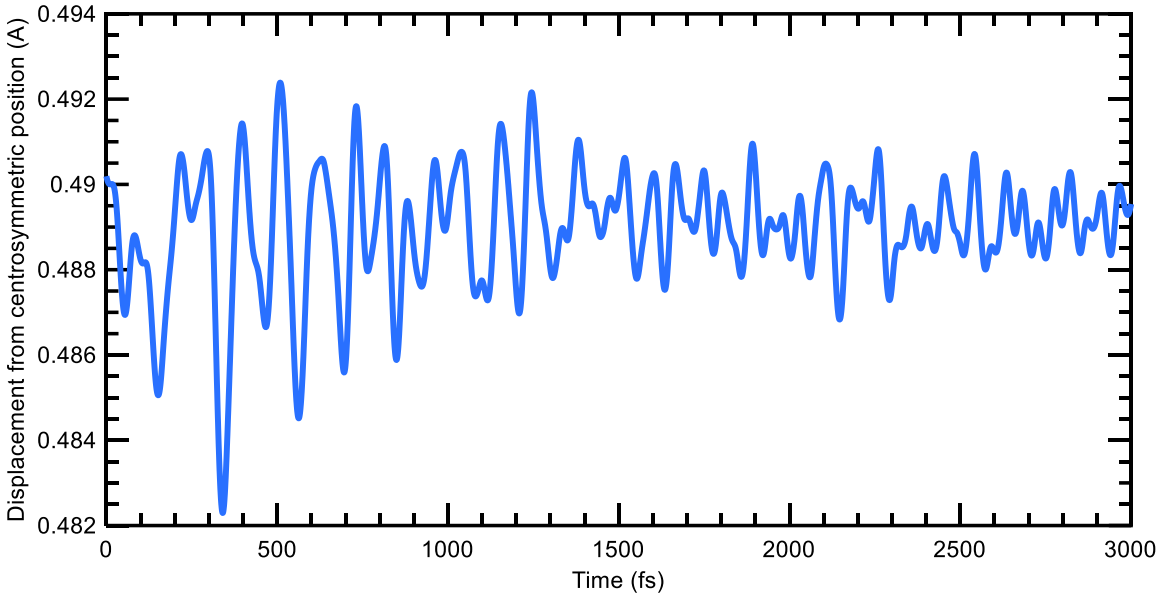

Fig. S5.1. Li atom displacement in the polar metal phase of $LiOsO_3$ upon excitation at t=0 fs with a 30-fs XFEL pulse. 3-ps molecular dynamics simulations were performed to track the Li atom position upon excitation of the polar metal phase of $LiOsO_3$ with a 30-fs XUV laser pulse. Over the course of the 3-ps experiment, the Li displacement relative to the nonpolar phase is 0.4881 +/- 0.0036 Å.

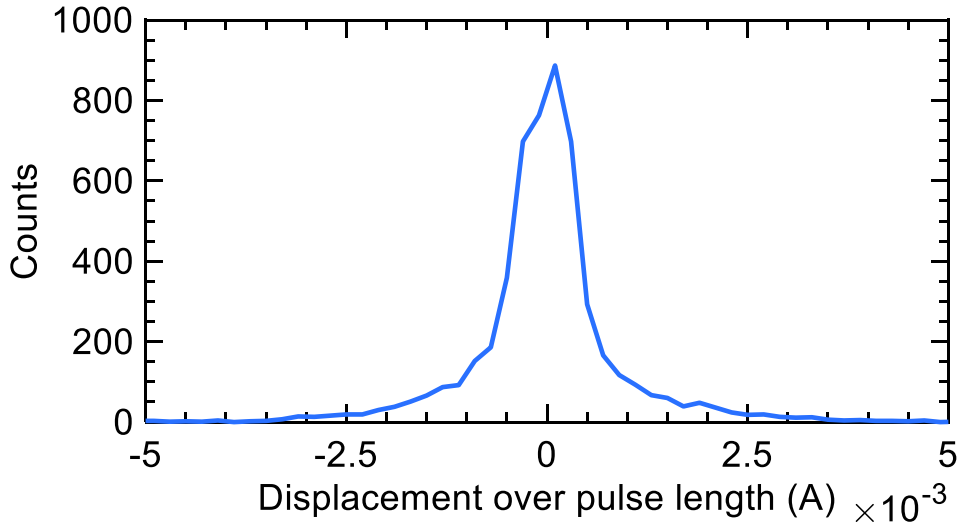

Fig. S5.2. Histogram reporting on the Li atom displacement in the polar metal phase relative to the non-polar phase of $LiOsO_3$ during the duration of the 30-fs pulse length. Upon sorting the displacements of **Fig. S5.1** within the 30-fs envelope of the incident light pulse, fluctuations in the Li atom displacement is seen to be less than 1% of its mean value. As such, SHG from these transient fluctuations due to the XFEL pulse itself can be reasonably neglected.

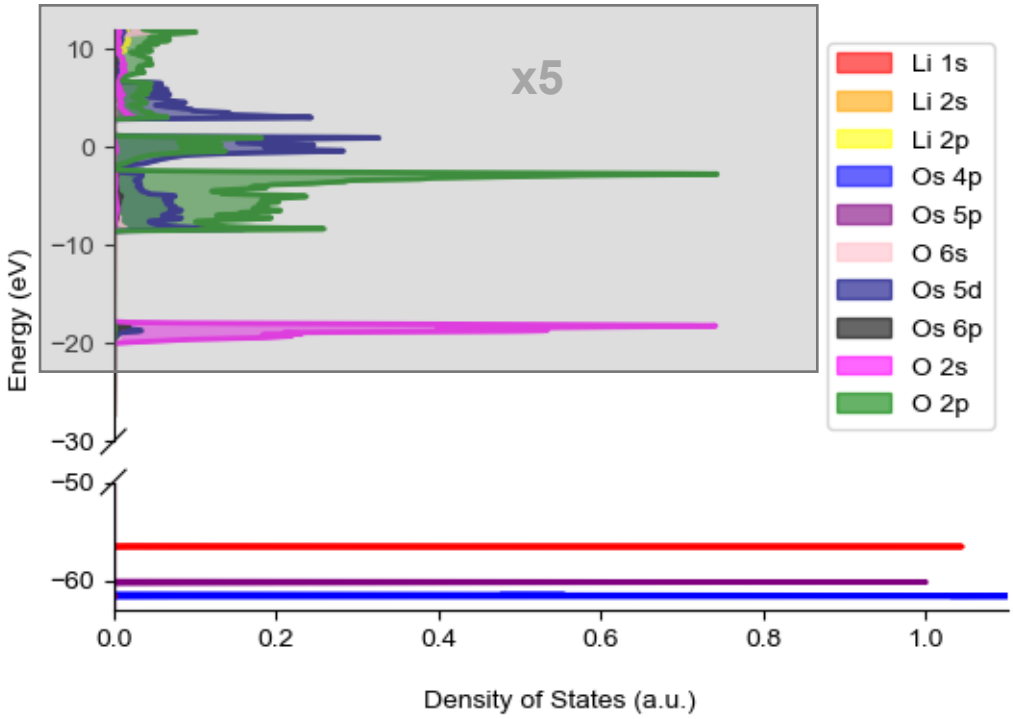

Fig. S6.1. Partial density of states of $LiOsO_3$ determined by DFT.

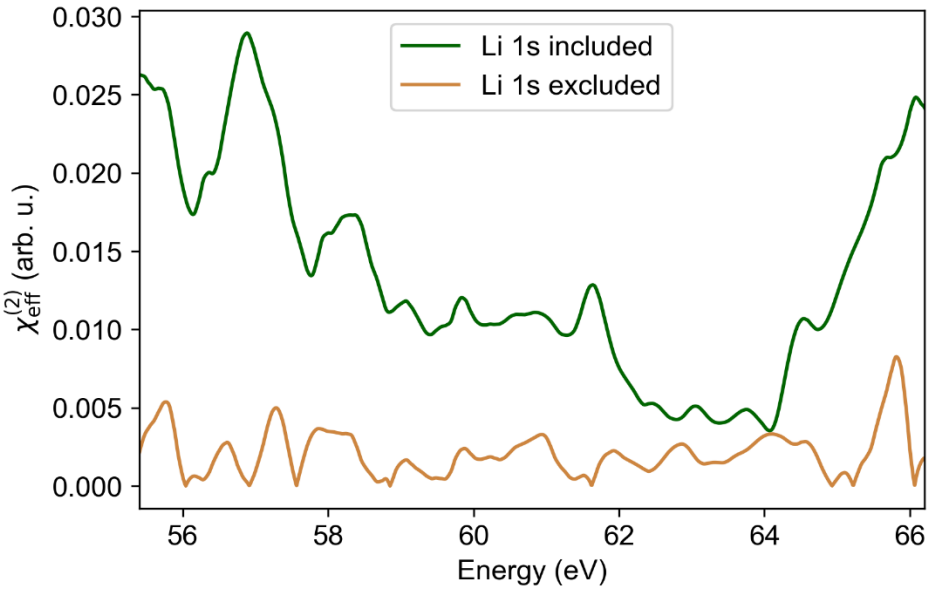

Fig. S7.1: $\chi^{(2)}_{eff}$ across the Li K-edge comparison between systems with and without Li 1s electron contribution. It can be seen that the response at 57 eV is due to the Li 1s core, as this response is not present when the Li 1s core is absent.

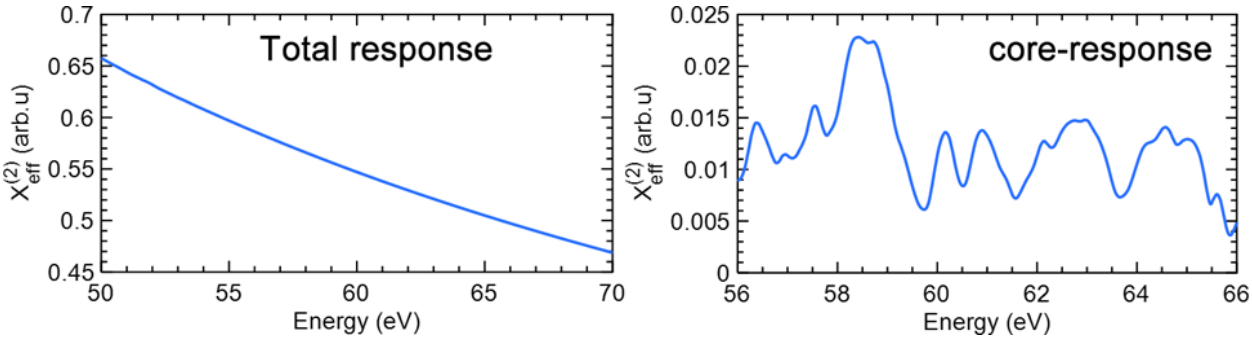

Fig. S8.1: $\chi^{(2)}_{eff}$ across the Li K-edge with (a) and without (b) background valence subtraction.

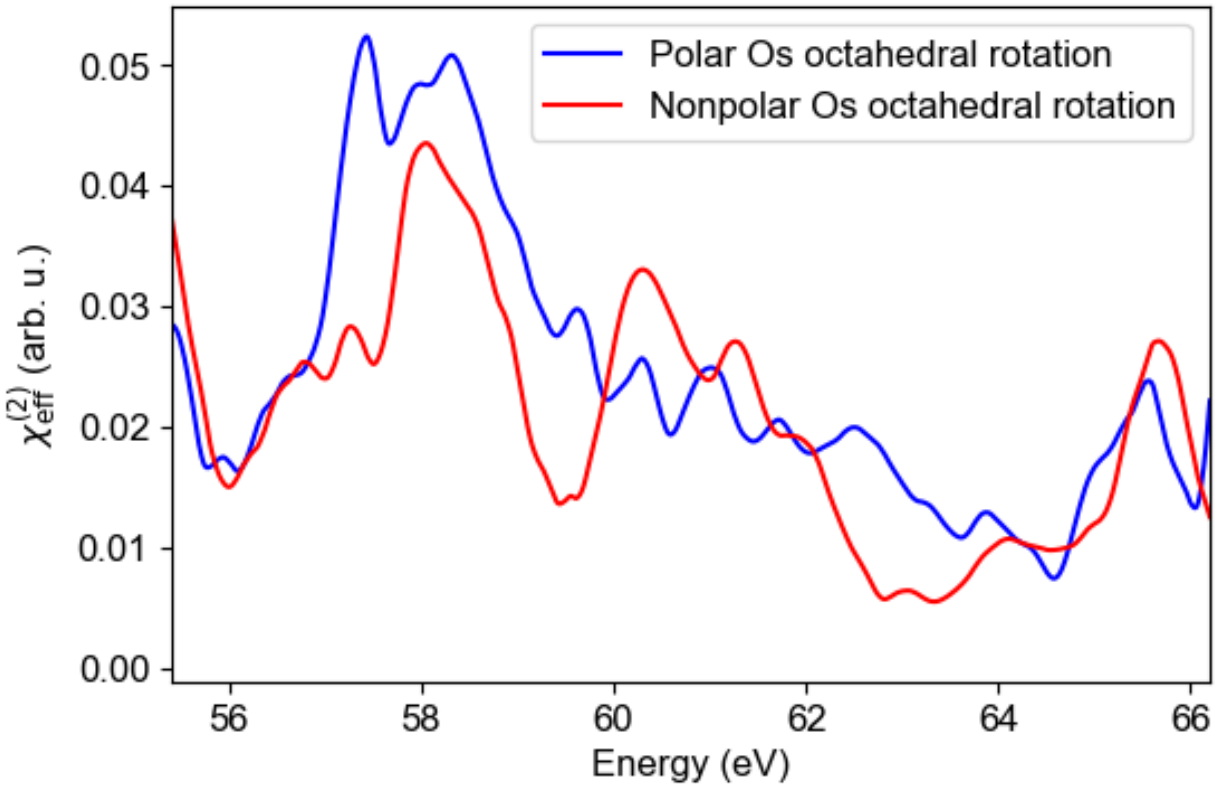

Fig. S9.1: $\chi^{(2)}_{eff}$ across the Li K-edge comparison between systems polar and nonpolar OsO_6 geometrical orientation.